





C/N/CeO₂/Alpha-Fe₂O₃ Doped Mesoporous Carbon as A Photocatalyst Material for Hydrogen Gas Production by Water Splitting Method

Nabilah Dita Anaqah¹ , Reza Ardiyanti Rahman¹ , Mintang Mulyanto¹ , Lioz Alexander¹ ,
Andi Fitri Ayu Lestari¹ , Riki Subagyo¹ , Yuly Kusumawati^{1*} 

¹Department of Chemistry, Faculty of Science and Data Analytics, Institut Teknologi Sepuluh Nopember, Kampus ITS Keputih, 60111, Sukolilo, Surabaya, Indonesia.

Abstract: This study focuses on hydrogen production through a water-splitting photocatalytic reaction using solar energy and an additional semiconductor material C/N/CeO₂/α-Fe₂O₃ as a photocatalyst. The semiconductor material C/N/CeO₂/α-Fe₂O₃ underwent thorough characterization via FTIR, FESEM-EDX, XRD, N₂ adsorption-desorption, and UV-Vis-DRS analysis. Subsequently, photocatalytic activity tests were conducted to measure hydrogen production levels for varying weight percentages of C/N/CeO₂/α-Fe₂O₃, including 0%, 10%, and 15 mass% of the C/N component. Results showed that the material with 0% variation produced 2.21 μmol/gram of hydrogen gas (1 hour) and 17.58 μmol/gram (after 3 hours), while the 10% variation yielded 4.52 μmol/gram (1 hour) and 19.08 μmol/gram (after 3 hours). These findings suggest that the C/N/CeO₂/α-Fe₂O₃ material containing 10% C/N may offer the most optimal performance as a photocatalyst for hydrogen production.

Keywords: Renewable Energy, Photocatalytic Water Splitting, Hydrogen Production, C/N/CeO₂/α-Fe₂O₃.

Submitted: November 25, 2023. **Accepted:** April 30, 2024.

Cite this: Anaqah ND, Rahman RA, Mulyanto M, Alexander L, Lestari AFA, Subagyo R, Kusumawati Y. C/N/CeO₂/Alpha-Fe₂O₃ Doped Mesoporous Carbon as A Photocatalyst Material for Hydrogen Gas Production by Water Splitting Method. JOTCSA. 2024;11(3): 995-1004.

DOI: <https://doi.org/10.18596/jotcsa.1395875>

***Corresponding author's E-mail:** y_kusumawati@chem.its.ac.id

1. INTRODUCTION

According to British Petroleum's statistical evaluation of the world energy in 2021, in 2020, 83%, 12.6%, and 6.3% of the world's energy consumption came from fossil fuels, nuclear energy, and renewable energy sources (mostly solar, wind, and water). Increased demand has led to increased use of fossil energy sources, which has led to the depletion of fossil energy reserves (1). Therefore, every country in the world must immediately initiate a significant energy transition to address future environmental and economic challenges (2).

Hydrogen is considered one of the primary candidates to meet future energy needs (3-5). Hydrogen is classified into three types: gray, green, and blue. Gray hydrogen, the most prevalent type currently, is derived from natural gas with high CO₂ emissions. Green hydrogen is produced from water using renewable energy sources, emitting no CO₂. Blue hydrogen is akin to gray hydrogen but incorporates CO₂ capture and storage (6). Green hydrogen as an alternative fuel for the shipping industry (7). One of the challenges in utilizing hydrogen (H₂) as future energy is to produce it from

clean sources (8). Hydrogen production is divided into conventional and renewable technologies, with conventional methods relying on fossil fuel processing like steam reforming, partial oxidation, and auto-thermal reforming, while renewable technologies focus on sources such as water or biomass (9).

Water splitting is a promising method for producing hydrogen from a clean source (10). This method offers both environmental and economic benefits over water electrolysis, utilizing solar energy to produce hydrogen with high conversion efficiency through a clean energy approach, thus avoiding greenhouse gas emissions (11). The process of water splitting involves harnessing one of the most abundant, clean, and limitless resources available. When the energy used to separate water is derived from renewable or low-carbon sources, the resulting hydrogen is known as green hydrogen (12).

The photocatalytic process of water splitting requires a semiconductor as the primary catalyst that uses light energy, particularly sunlight, to split water molecules into hydrogen and oxygen. Semiconductors as catalysts are essential in

capturing light energy, stimulating water degradation, and facilitating these chemical reactions (13). Therefore, the semiconductors are a must to synthesize for these reactions to work.

The semiconductor commonly used in photocatalytic applications is titanium dioxide (TiO_2) because of its excellent optical and electronic properties, high chemical stability, low cost, non-toxic, and environmentally friendly (14). However, one of the main weaknesses of TiO_2 is that the band gap is relatively large, 3.2 eV, which means that TiO_2 only absorbs ultraviolet (UV) light and a small fraction of visible light (15). In addition, the rapid recombination between electrons (e^-) and holes (hole, h^+) leads to the loss of energy that can be used to trigger the desired chemical reaction, thereby reducing the efficiency of photocatalysis (16).

The $\alpha\text{-Fe}_2\text{O}_3$ material (ferric oxide or hematite) is a material that has the potential as a photocatalytic semiconductor material (17). Hematite has a band gap width of 2.1 eV, which is smaller than TiO_2 , the ability to generate electron-hole pairs when exposed to light, and chemical stability suitable for various reaction environments (18). An Organic Structure-Directing Agent (OSDA) in synthesizing $\alpha\text{-Fe}_2\text{O}_3$ is an approach to align the alpha structure. Methylene blue acts as a template molecule in the synthesis of $\alpha\text{-Fe}_2\text{O}_3$ photocatalyst and as a target of aromatic compounds in photocatalytic degradation. However, $\alpha\text{-Fe}_2\text{O}_3$ has a high recombination rate because it has a concise hole diffusion path (around 2–4 nm) as well as a low oxidation ability, which leads to a reduction in the amount of hydrogen without reducing the coke rate (19). To solve the laxity of $\alpha\text{-Fe}_2\text{O}_3$, active materials with a large surface area are needed. One approach is to dope $\alpha\text{-Fe}_2\text{O}_3$ with other materials. Doping is one of the most crucial modification strategies to adjust the band gap of existing photocatalysts and reduce the carrier recombination rate (20).

Cerium oxide (CeO_2) is widely used in photocatalysis because it is an electron acceptor and can facilitate oxidation-reduction reactions (21). CeO_2 material exhibits chemical stability in various environments and energy conversion efficiency in various photocatalytic applications. Its advantage lies in cerium's ability to absorb oxygen, which allows it to release oxygen in reducing conditions and store it when it fills the oxygen space in oxidizing conditions (22). CeO_2 materials are commonly combined with other semiconductors and surface modifications to improve performance in solar energy conversion and photocatalytic reactions (23).

The presence of lattice oxygen, oxygen vacancies, or defects in the crystal lattice of a material such as CeO_2 can play an important role in photocatalytic performance (24). More oxygen vacancies in the CeO_2 lattice generally increase its ability to participate in redox reactions such as $\text{Ce}^{4+}/\text{Ce}^{3+}$ and $\text{Fe}^{2+}/\text{Fe}^{3+}$. This increases its reactivity and photocatalytic performance. However, care must be taken to ensure that chemical reactions do not lead to undesirable side effects (25). A practical approach to minimize the side effects caused by

lattice oxygen is to modify the photocatalyst material (26).

Nitrogen and carbon doping can help reduce side effects that can occur due to the presence of oxygen vacancies in materials such as CeO_2 . This can improve the control and stability of chemical reactions (27). Doping carbon with nitrogen has been shown to improve photocatalytic performance by promoting charge delocalization and surface modification of carbon. Combining these two dopants in CeO_2 makes properties more suitable for applications such as photocatalysis (28).

In this research, the $\alpha\text{-Fe}_2\text{O}_3$ photocatalyst material was modified with C/N/ CeO_2 , resulting from modifying CeO_2 with N-doped carbon. The materials C/N/ CeO_2 and C/N/ $\text{CeO}_2/\alpha\text{-Fe}_2\text{O}_3$ were synthesized via the hydrothermal method. The hydrothermal method has been chosen because this method can be conducted in mild operating conditions and the crystallite size and purity can be controlled (29-30). The resulting C/N/ $\text{CeO}_2/\alpha\text{-Fe}_2\text{O}_3$ composite was confirmed by a series of characterizations, including UV-Vis diffuse reflections measurement to determine band gap energy, X-Ray diffraction for knowing structure and crystal phase of the material, Fourier-Transform Infra-Red spectroscopy measurement find the functional groups of material, Field Emission Scanning Electron Microscopy for explain surface morphology dan atom distribution, GC-TCD to analyze the components of complex mixtures and detect all molecules including hydrogen, which is then followed by a photocatalytic effectiveness test, and N_2 adsorption-desorption isotherm to find out surface area and pore distribution. In addition to these characterizations, photocatalytic activity tests were also carried out to determine the evolution of the hydrogen produced. Modifying $\alpha\text{-Fe}_2\text{O}_3$ with C/N/ CeO_2 is expected to increase the photocatalytic activity, thermal and chemical stability, and surface area of the photocatalyst material. The large surface area of the photocatalyst material creates active centers, which also increases hydrogen production. Hopefully, this research can provide alternatives and scientific references to photocatalytic materials that are effectively used for hydrogen production through water splitting.

2. EXPERIMENTAL SECTION

2.1. Materials

The material used in this research was cerium(III) nitrate hexahydrate $\text{Ce}(\text{NO}_3)_3 \cdot 6\text{H}_2\text{O}$ (99.8% Sigma-Aldrich), iron (III) chloride FeCl_3 (99%, Merck), methylene blue (99 %, Merck), ethanol (99.9%, Merck), N_2 gas (>99.99%, UHP), glycine (99%, Sigma-Aldrich), ammonium hydroxide NH_4OH (25%, Merck), distilled water (H_2O), urea $\text{CO}(\text{NH}_2)_2$ (99%, Merck), 500 mesh commercial activated carbon, sodium hydroxide NaOH (99.9%, Merck) and methanol (99.9%, Merck).

2.2. Synthesis of Nitrogen-Doped Mesoporous Activated Carbon (C/N)

5.04 g of commercial activated carbon was purchased and used without any purification and was added to 250 mL of 2 M urea solution made from $\text{CO}(\text{NH}_2)_2$ and distilled water stirred with a

magnetic stirrer at 35 °C for 24 hours. The samples were then dried at 105 °C for 6 hours. After the sample was dried, it was activated in a tube furnace supplied with N₂ gas at a temperature of 450 °C for 50 minutes.

2.3. Synthesis of C/N-doped CeO₂ (C/N/CeO₂)

The synthesized N-doped mesoporous activated carbon was then grouped with weight percent variations of 10 and 15 mass%. Each was added to 10 mL of distilled water by ultrasonication for 30 minutes until a black suspension was obtained. Afterwards, 15 mL of a 0.1 M (Ce(NO₃)₃·6H₂O) was added to the suspension and stirred with a magnetic stirrer for 15 minutes. Then, 2 M NaOH was added dropwise to the mixture until the pH reached 10-12. The mixture was stirred with a magnetic stirrer for one hour. The sample was placed in a hydrothermal autoclave at 180 °C for 24 hours. The hydrothermal results were decanted, and then the precipitate was dried in an oven at 60 °C for 12 hours.

2.4. Synthesis of α-Fe₂O₃

The synthesis of the α-Fe₂O₃ material was carried out by dissolving 0.41 g of glycine, 0.025 g of methylene blue, and 5.04 g of FeCl₃·6H₂O in 10 mL of distilled water and stirring with a magnetic stirrer for 30 min. Add 5 mL of NH₄OH to the solution while stirring again. After adding NH₄OH, the solution was placed in a hydrothermal autoclave and heated at 160 °C for 10 hours. The mixture resulting from the hydrothermal process is left to stand at room temperature and then decanted to separate the filtrate and sediment. The resulting brick-red solid was then centrifuged using distilled water and ethanol as solvent to remove impurities. Then, the centrifugation results were decanted again to remove the precipitate and dried at 80 °C for six hours. The solid was then calcined under N₂ gas at 450 °C for three hours.

2.5. Synthesis of C/N/CeO₂/α-Fe₂O₃

After obtaining the C/N/CeO₂ and α-Fe₂O₃ materials, the synthesis of C/N/CeO₂/α-Fe₂O₃ was continued using a hydrothermal process with variations (0, 10, and 15 mass%). A total of 0.33 grams of N/CeO₂-doped mesoporous carbon composite was dissolved in 7.5 mL of distilled water and stirred for 30 minutes. Then, 0.65 grams of α-Fe₂O₃ was dissolved in 20.3 mL of distilled water and added to the N/CeO₂ mixture. The mixture was stirred for 1 hour. The obtained samples were placed in a hydrothermal autoclave and heated at 140 °C for five hours and then left at room temperature. The solid obtained at the end of the synthesis is C/N/CeO₂/α-Fe₂O₃ as the photocatalyst material with 0, 10, and 15 mass% compositions C/N. The higher the weight percentage of C/N added, the darker the product color obtained. The mass of products produced includes C/N/CeO₂/α-Fe₂O₃ 0 mass%, C/N/CeO₂/α-Fe₂O₃ 10 mass% and C/N/CeO₂/α-Fe₂O₃ 15 mass% in order are 0.4478; 0.4432; and 0.4452 grams.

2.6. Material Characterization

Several instruments were used to characterize C/N/CeO₂/α-Fe₂O₃ such as Fourier Transform Infrared Spectrophotometer (FTIR, Shimadzu, $\nu = 400-4000$ cm⁻¹), Field Emission Scanning Electron Microscopy with Energy Dispersive X-ray Spectroscopy (FESEM-

EDX,) and X-Ray Diffraction (XRD, $2\theta = 20-90^\circ$) where these three instruments are used to determine the structure properties of the material. Brunauer-Emmett-Teller (BET) and Barrett Joyner Halenda (BJH) are used to obtain the surface area and the pore size of the material, UV-Vis Diffuse Reflectance spectrophotometer (UV-DRS, Agilent Cary 60, $\lambda = 200-800$ nm) is used to analyze the band gap of the material.

2.7. Photocatalytic Activity Test

The photocatalytic activity test was conducted in the Centre of Advanced Material and Energy Sciences, Universiti Brunei Darussalam, Brunei Darussalam. Osram Powerstar lamp was employed as a light source. A 20 mg of catalyst was dispersed in a 25 mL aqueous solution containing 20% of methanol. To provide visible light, a UV filter was conducted during irradiation. An irradiation chamber, Opsytec BS-02, was used to have a stable temperature and light intensity. The temperature inside the irradiation chamber was measured during the photocatalytic reaction at ~40-50 °C. The light intensity was measured using LI-COR light meter Model LI-250A. The hydrogen production was collected by gas syringe after 1-hour and 3-hour irradiation. The collected gas was then analyzed via gas chromatography, Shimadzu GC-2014, with a thermal conductive detector (TCD).

3. RESULTS AND DISCUSSION

The FTIR spectrum of activated carbon and the synthesis results of nitrogen-doped activated carbon in Figure 1a show that the absorption peak at wave number 1078 cm⁻¹ is associated with the C=O group, and the peak at 1539 cm⁻¹ is associated with the stretching of the C-OH single bond. After nitrogen doping, the absorption peak shifted red to 1026 and 1537 cm⁻¹. This shows that the structure of the mesoporous carbon changed with the addition of nitrogen. The particular band peak still present after N-doped carbon indicates no damage from urea impregnation (24).

After the nitrogen-doped activated carbon material (C/N) was obtained, the material was doped with CeO₂ in variations of 0, 10, and 15 mass%. The addition of CeO₂ doping to C/N Figure 1b gives several absorption bands which are 450 cm⁻¹, 1360 cm⁻¹, 1640 cm⁻¹ and 3470 cm⁻¹. The absorption bands 474 and 484 cm⁻¹ indicate the presence of stretching vibrations in CeO₂, the absorption at 1643 cm⁻¹ indicates the presence of bending bonds (H-O-H), and the absorptions at 3475 and 3473 cm⁻¹ indicate the presence of -OH bonds caused by water absorption during the synthesis process. The specified variations affect the spectra results, as indicated by differences in peak sharpness in each spectrum. In Figure 1c, you can see the characterization results of the C/N/CeO₂/α-Fe₂O₃ material for variations of 0, 10, and 15 mass%. of the C/N weight. The absorption bands 484 and 580 cm⁻¹ show the characteristic properties of α-Fe₂O₃ and CeO₂ compounds. The absorption at 1637 cm⁻¹ indicates the presence of the C-N functional group. Based on the characterization results, the C/N/CeO₂/α-Fe₂O₃ material varies in 0, 10, and 15 mass%. was successfully synthesized.

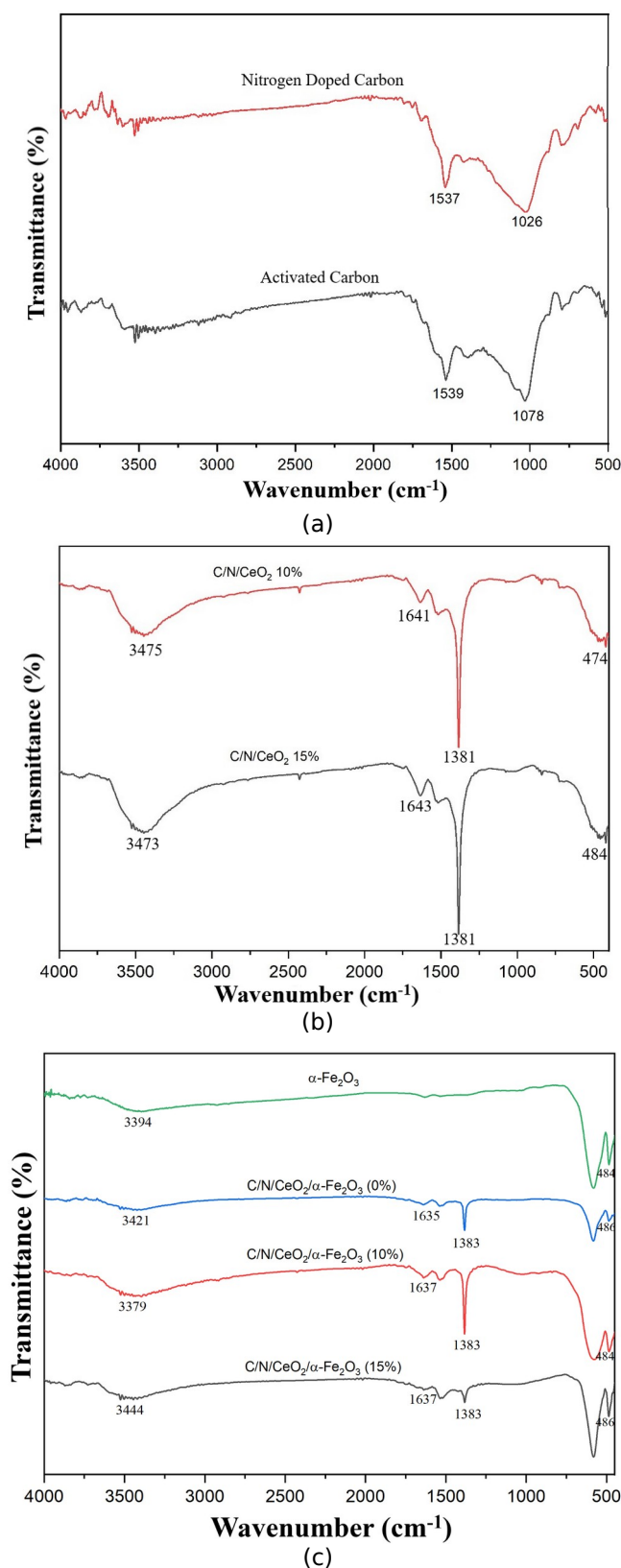


Figure 1: (a) FTIR results of activated carbon and nitrogen-doped activated carbon and (b) FTIR results of C/N/CeO₂ 10 and 15 mass%., and FTIR results of α -Fe₂O₃ and (c) C/N/CeO₂/ α -Fe₂O₃ (0, 10 and 15 mass%).

Results of FESEM-EDX characterization of C/N, α -Fe₂O₃, and C/N/CeO₂/ α -Fe₂O₃ materials at 10 mass% and its morphology can be observed in Figures 2a, b, and c. The FESEM results of the C/N material showed porous structural morphology and many small particles around the pores caused by the

carbonization process (29). The EDX results of C/N show the distribution of C atoms in red, O atoms in green, and N atoms in orange. The distribution of elements and morphology indicate that N-doped mesoporous carbon was successfully synthesized. The FESEM characterization results of α -Fe₂O₃ show

that the material's morphology is hollow and porous due to the addition of the structure-directing agent methylene blue. After doping, the FESEM results show C/N/CeO₂/α-Fe₂O₃ 10 mass%. Shows that the morphology of the initially porous material was covered by dopant material. This is because the

addition of C/N causes the pores to be closed by the catalyst. EDX results of α-Fe₂O₃ and C/N/CeO₂/α-Fe₂O₃ materials at 10 mass%. The difference in atom distribution lies in the blue Ce atoms and the red C atoms in C/N/CeO₂/α-Fe₂O₃ 10 mass%.

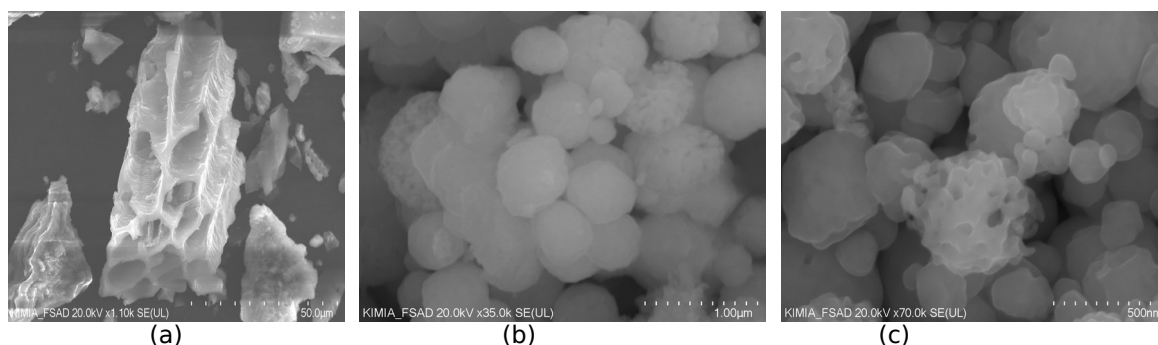


Figure 2: (a) FESEM-EDX C/N (b) Fesem-EDX α-Fe₂O₃ and (c) FESEM-EDX C/N/CeO₂/α-Fe₂O₃.

The sample diffractogram results were monitored at an angle of 2θ from the range (20–90) using a Cu Kα light source (λ = 1.54060 Å). The results of the diffractogram pattern of C/N/CeO₂/α-Fe₂O₃ (0, 10 and 15 mass%) shown in Figure 3 show that the sample results have a hematite phase with a diffraction peak of 2θ = 33.2; 35.7; 40.9; 49.7; 54.3; 62.4; and 64° with Miller indices (1 0 4), (1 1 0), (1 1 3), (0 2 4), (1 1 6), (2 1 4), (3 0 0) from the JCPDS database code (84-0311) (20). In addition, Figure 3 shows the crystalline phase diffraction peaks 2θ = 47.6 and 56.5°, which correspond to the Miller index

(2 2 0), (3 1 1) from the JCPDS database code (34-0394), indicating this, that the peak nano-large formations were formed from the pure cubic CeO₂ phase (30). The diffractogram results at diffraction peak 2θ = 28.6° showed that nitrogen-doped mesoporous carbon in the diffractograms of C/N/CeO₂/α-Fe₂O₃ (10 mass%) and C/N/CeO₂/α-Fe₂O₃ (15 mass%), while the diffractogram of C/N/CeO₂/α-Fe₂O₃ (0 mass%) does not contain a diffraction peak at 2θ = 28.6°. Based on the characterization results, the C/N/CeO₂/α-Fe₂O₃ material varies between 0, 10, and 15 mass%. was successfully synthesized.

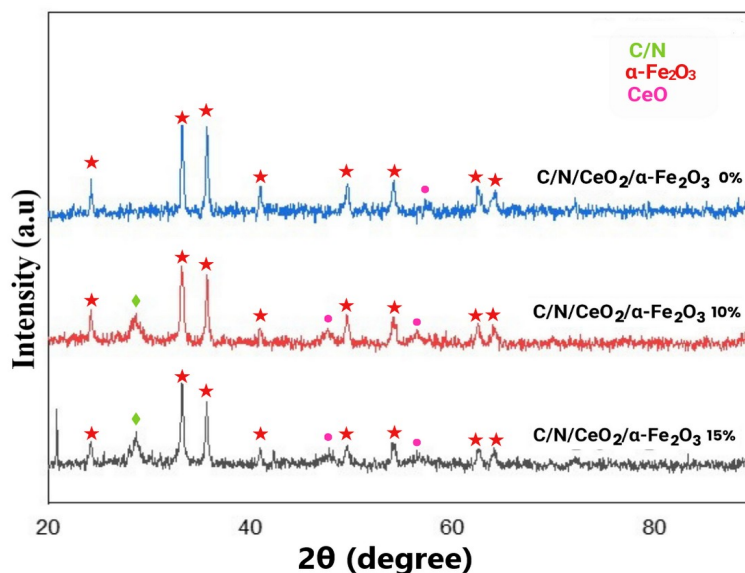


Figure 3: Diffractogram results of C/N/CeO₂/α-Fe₂O₃ (0, 10 and 15 mass%).

The nitrogen adsorption-desorption isotherm was measured at -195.85 °C. The samples were prepared under vacuum conditions (10⁻⁴ Torr) at a temperature of 150 °C. The surface area is calculated from the adsorption isotherm branch by applying the BET equation using a single point. The pore size distribution was estimated using the BJH method from the desorption branch. The results of C/N nitrogen adsorption-desorption characterization showed a BET surface area of 203.84 m² /g with a

pore size of 4.95 nm, as shown in Figure 4a. Figure 4b shows the C/N sample has an H₄ hysteresis-type loop. These results indicate that the C/N material has a mesoporous structure. The desorption branch for H₄ hysteresis-type pores at low P/P₀ 0.1 indicates that the desorption process does not reach the same level as the adsorption process. The pores remain partially filled after the desorption process is complete (29).

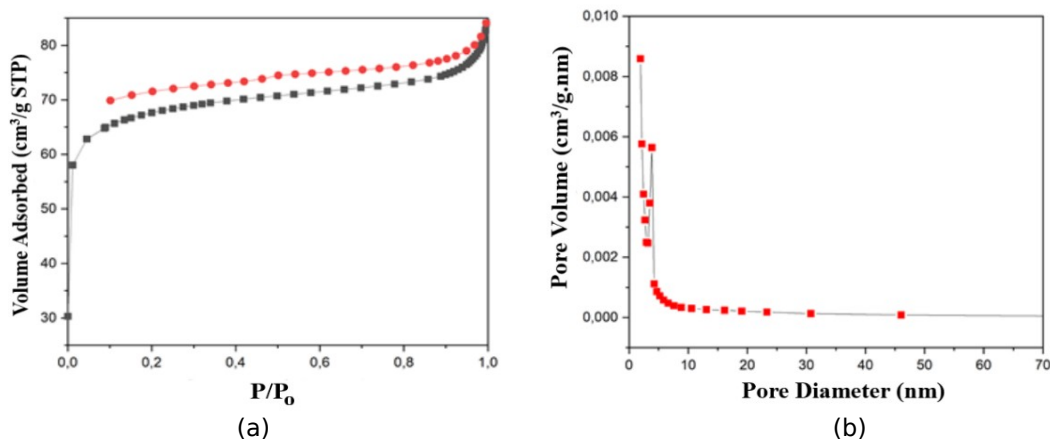


Figure 4: (a) C/N nitrogen adsorption-desorption isotherm and (b) pore size distribution.

UV-Vis DRS tests provide information in a wavelength spectrum versus R or reflectance (%). The band gap energy is obtained by converting the R% to the Kubelka-Munk factor (31). Materials exposed to photons partially absorb, reflect, and transmit bandgap energy. The results of the UV-Vis DRS test show that the more C/N present in the photocatalyst material, the less energy is required. Based on the Kabelka-Munk relationship with

energy, the photocatalyst material varies by 0 mass %. Figure 5a, C/N has a band gap energy of 1.98 eV and a variation of 10 mass%. Figure 5b has a band gap energy of 1.9 eV while at a variation of 15 mass %. Figure 5c produces a band gap energy of 1.69 eV. These results suggest that the variation ranges from 0 to 15 mass %. With the C/N composition, the resulting band gap energy decreases and moves into the visible light region (32).

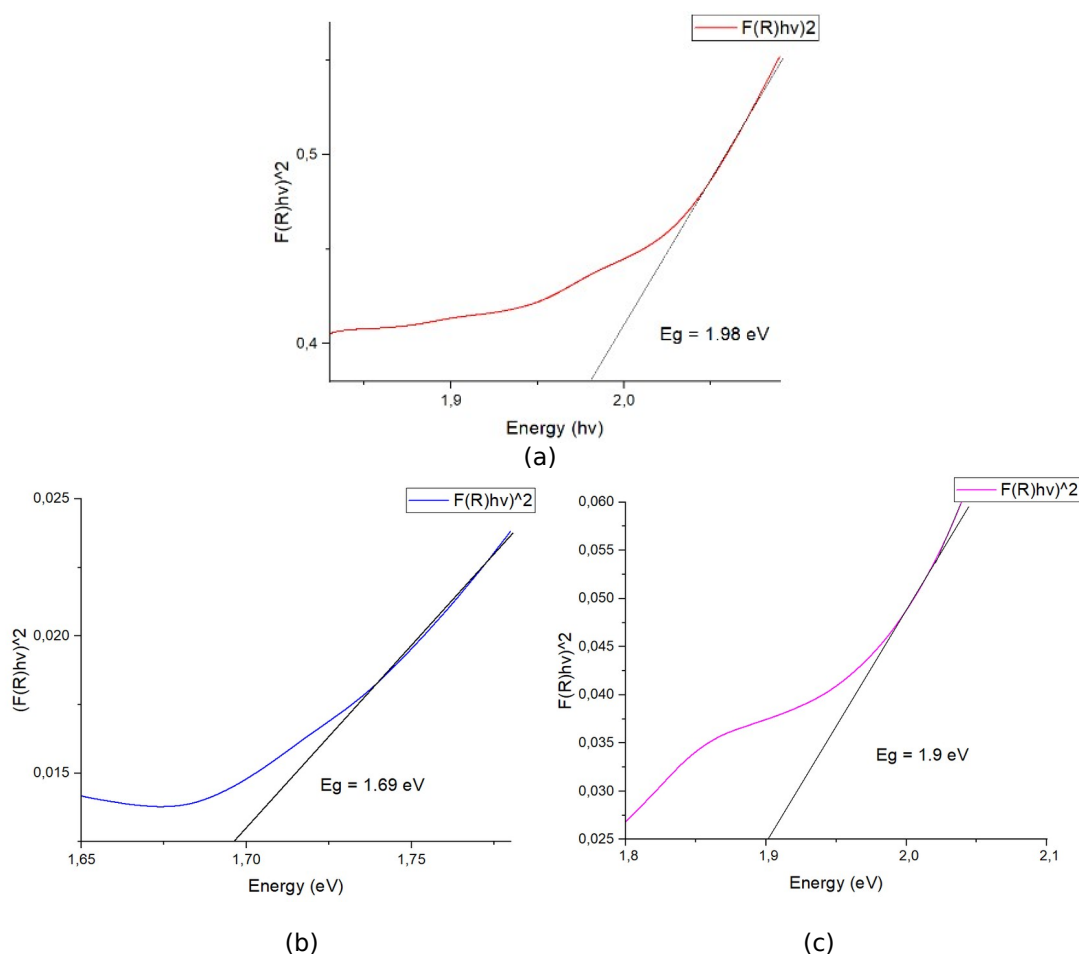


Figure 5: UV-Vis DRS (a) C/N 0 mass%, (b) C/N 10 mass%, (c) C/N 15 mass%.

The addition of C/N is used as an anionic dopant, which can reinforce the weakness of CeO₂ as an inhibitor of coke and recombination rates (33). The C/N material has active centers due to the presence of electron pairs from the N atom, which can

weaken the O-O bond. This increases the photocatalytic activity as an oxygen reduction reaction takes place. The dipole-dipole interaction formed by bonding carbon atoms to nitrogen shows a higher positive charge density and stronger

electron affinity. However, adding nitrogen-doped carbon in an excessive ratio can limit the catalytic activity. This is because the active N site is coated with carbon (34). Figure 6 shows that the more C/N

is added to the photocatalyst material, the higher the generated reflection intensity. It can be assumed that more light is absorbed with the higher reflected intensity.

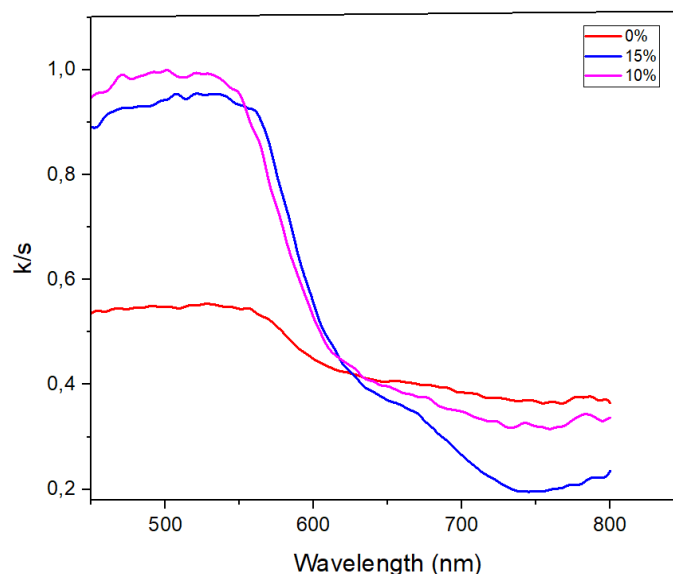


Figure 6: UV-Vis DRS spectra wavelength to reflectance (%) of C/N in every variation.

The photocatalytic activity test for hydrogen production was carried out using a GC-TCD device. The photocatalyst solid was weighed up to 50 mg and then dispersed in 25 mL of 20% methanol solution. The mixture was stirred for 10 minutes and

then ultrasonicated for 10 minutes. Argon gas was then flowed through the mixture for 5 minutes. The solution was placed in a photocatalytic reactor and irradiated with UV light for 3 hours (Figure 7).

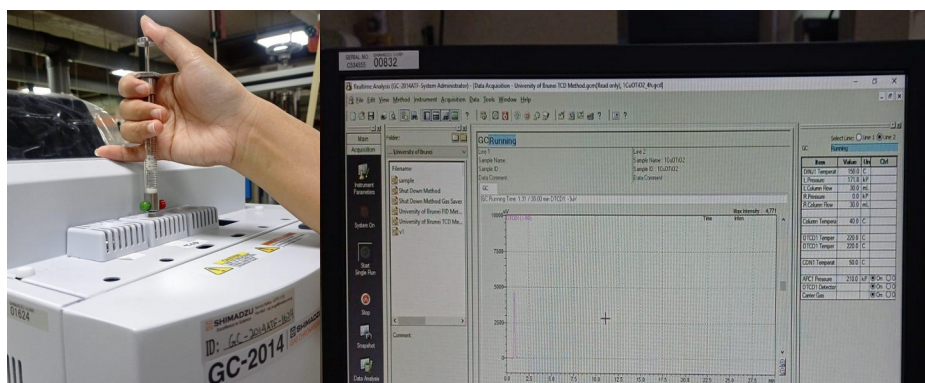


Figure 7: GC-TCD Device for measure the hydrogen gas formed in this experiment.

The hydrogen gas formed is then removed with a syringe and introduced into the GC-TCD device for the analysis process. The results of hydrogen gas amount obtained within 1 and 3 hours with

variations in C/N/CeO₂/α-Fe₂O₃ (C/N 0, 10 and 15 mass%). The equation used to measure the amount of hydrogen in the syringe is as follows

$$\text{Volume of } H_2 \text{ in reaction bottle} = \frac{\text{Volume of } H_2 \text{ in syringe} \times 33.5 \text{ mL of headspace}}{0.5 \text{ mL of extracted } H_2 \text{ gas}} \quad (\text{Eq. 1})$$

It is known that the Volume of Hydrogen in Syringe/mL comes from the peak divided by the hydrogen calibration results.

Photocatalyst material C/N/CeO₂/α-Fe₂O₃ variation 0 mass%. gives results for the amount of hydrogen production in 1 hour of 2.21 μmol/g and after 3 hours of 17.58 μmol/g (Figure 8). Photocatalyst material C/N/CeO₂/α-Fe₂O₃ variation 10 mass% gave

optimal results with an amount of hydrogen production in 1 hour of 4.2 μmol/g and after 3 hours of 19.08 μmol/g. Adding composition variations of 15 mass % material does not produce hydrogen gas in visible light. This may be caused by the surface and pore structure of C/N having covered the active site of the catalyst and the band gap energy is 1.69 eV, leading to the solar radiation-based infrared light region. According to research

data by Dao et al (2023) (35), hydrogen production with $\alpha\text{-Fe}_2\text{O}_3$ doped and undoped NGr material resulted in hydrogen production amounts of 1.95

$\mu\text{mol}/\text{mg}\cdot\text{h}$ and $0.39 \mu\text{mol}/\text{mg}\cdot\text{h}$. This indicates that the addition of C/N/CeO₂ doping can increase the photocatalytic efficiency.

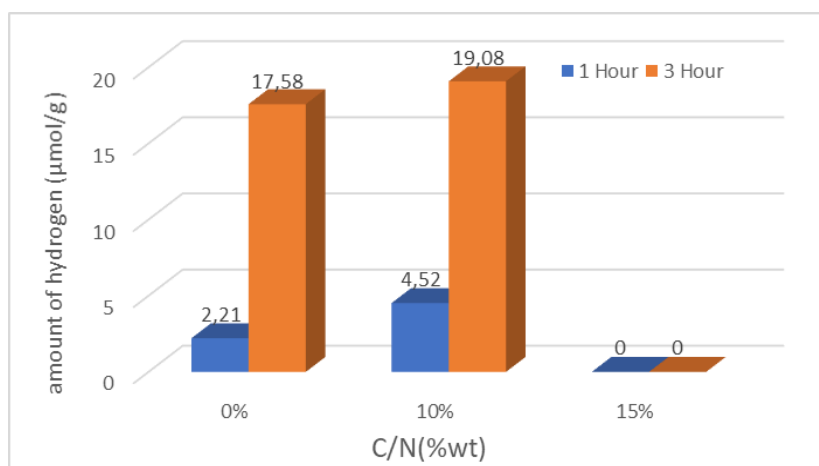


Figure 8: Hydrogen production by variation of C/N content within 1 and 3 hours.

The consideration of an optimal photocatalytic system for H₂ involves physical processes. The

entire chemical process is represented in the following figure.

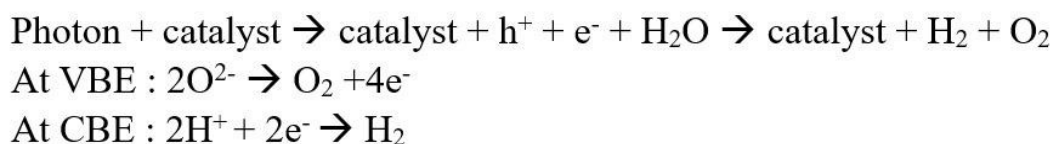


Figure 10: General mechanism of hydrogen gas production.

The development of electrical semiconductor settings has made a significant contribution to the operational efficiency of photocatalysis processes. Semiconductors are differentiated from conductors based on two main bands, namely the valence band (VB) and conduction band (CB), with an energy difference (E_g) that differentiates the two. The activation process ensures that electrons and holes are only found in the valence band. To excite a semiconductor, the incoming light energy must be equal to or higher than the band gap energy. When photons excite electrons from the valence band to the conduction band, holes are formed in their place. The mechanism of photocatalytic air mechanization of alpha semiconductor Fe₂O₃/CeO₂/C/N involves certain steps. In the initial

stage, electrons and holes are created when light hits the semiconductor surface. The energy released can be in the form of heat or photons when electrons and holes recombine quickly on the semiconductor surface. Additionally, electrons and holes can also be involved in chemical reactions, as illustrated in the equation below. Additionally, the photoexcited pairs can initiate chemical reactions at the semiconductor surface, with the holes reacting with H₂O molecules to produce the desired reaction products. In the final stage, electrons and holes produced from the photoexcitation process will take part in the reaction that produces O₂ and H₂O. This is a simple overview of the photocatalytic air separation process.

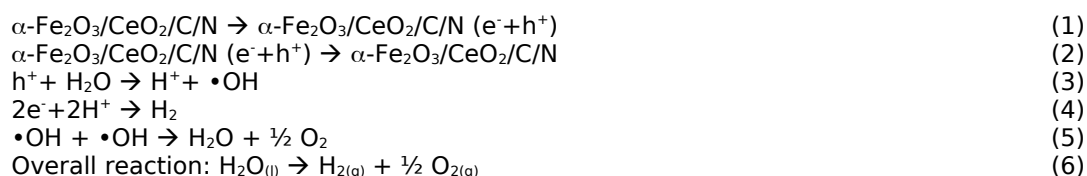


Figure 11: Mechanism of hydrogen gas production.

4. CONCLUSION

In this research, N-doped mesoporous carbon (pore size of 4.9260 nm and surface area 203,84 m²/g) was successfully synthesized as a CeO₂/α-Fe₂O₃ dopant via the hydrothermal method. The effect of doping composition variations N-doped mesoporous carbon 0, 10, and 15 mass% in photocatalytic

reactions for hydrogen gas production was investigated. Photocatalytic activity efficiency test results show that optimum C/N/CeO₂/α-Fe₂O₃ photocatalyst material with C/N variation 10 mass% for hydrogen production in 1 hour is 4.2 μmol/g and 19.08 μmol/g in 3 hours. After three hours, the hydrogen production fluctuation increased by 76.31%. In addition, the C/N mass percentage variation to the photocatalyst material affects the active catalytic sites and band gap energy. Based on the above description, it can be concluded that C/N/CeO₂/α-Fe₂O₃ has the potential to be used and developed as a photocatalyst for hydrogen production through the water-splitting reaction.

5. CONFLICT OF INTEREST

There is no conflict of interest.

6. ACKNOWLEDGEMENT

The authors gratefully acknowledge financial support from the Directorate General of Higher Education, Research and Technology, Ministry of Education, Research and Technology, Republic of Indonesia through the Student Creativity Program (PKM 2023). Dr. Hasliza Bahruzi from the Centre of Advanced Material and Energy Sciences, Universiti Brunei Darussalam, Brunei Darussalam is acknowledged for providing apparatus for photocatalytic activity.

7. REFERENCES

- Holechek JL, Geli HME, Sawalhah MN, Valdez R. A Global Assessment: Can Renewable Energy Replace Fossil Fuels by 2050? Sustainability [Internet]. 2022 Apr 16;14(8):4792. Available from: [<URL>](#).
- Welsby D, Price J, Pye S, Ekins P. Unextractable fossil fuels in a 1.5 °C world. Nature [Internet]. 2021 Sep 9;597(7875):230–4. Available from: [<URL>](#).
- Garzón Baquero JE, Bellon Monsalve D. From fossil fuel energy to hydrogen energy: Transformation of fossil fuel energy economies into hydrogen economies through social entrepreneurship. Int J Hydrogen Energy [Internet]. 2024 Feb 7;54:574–85. Available from: [<URL>](#).
- Marouani I, Guesmi T, Alshammari BM, Alqunun K, Alzamil A, Alturki M, et al. Integration of Renewable-Energy-Based Green Hydrogen into the Energy Future. Processes [Internet]. 2023 Sep 7;11(9):2685. Available from: [<URL>](#).
- Bilgic G, Bendes E, Ozturk B, Atasever S. Recent advances in artificial neural network research for modeling hydrogen production processes. Int J Hydr En. 2023; 48:18947–18977. Available from: [<URL>](#).
- Atilhan, S., Park, S., El-Halwagi, M. M., Atilhan, M., Moore, M., & Nielsen, R. B. (2021). Green hydrogen as an alternative fuel for the shipping industry. Current Opinion in Chemical Engineering, 31, 100668. <https://doi.org/10.1016/j.COCHE.2020.100668>.
- Marouani I, Guesmi T, Alshammari BM, Alqunun K, Alzamil A, Alturki M, et al. Integration of Renewable-

Energy-Based Green Hydrogen into the Energy Future. Processes. 2023 Sep 7;11(9):2685.

- Kaplan H, Şahin M, Bilgiç G. The Influence of Magnetic Field on Newly Designed Oxyhydrogen and Hydrogen Production by Water Electrolysis. Energy Technol [Internet]. 2021 Dec 10;9(12):2100617. Available from: [<URL>](#).
- Bilgiç G, Öztürk B. Modeling of Artificial Neural Networks for Hydrogen Production via Water Electrolysis. El-Cezeri J Sci Eng [Internet]. 2023 Jan 11;10(1):137–46. Available from: [<URL>](#).
- Hota P, Das A, Maiti DK. A short review on generation of green fuel hydrogen through water splitting. Int J Hydrogen Energy [Internet]. 2023 Jan 5;48(2):523–41. Available from: [<URL>](#).
- Ravi P, Noh J. Photocatalytic Water Splitting: How Far Away Are We from Being Able to Industrially Produce Solar Hydrogen? Molecules [Internet]. 2022 Oct 23;27(21):7176. Available from: [<URL>](#).
- Arsad AZ, Hannan MA, Al-Shetwi AQ, Begum RA, Hossain MJ, Ker PJ, et al. Hydrogen electrolyser technologies and their modelling for sustainable energy production: A comprehensive review and suggestions. Int J Hydrogen Energy [Internet]. 2023 Aug 22;48(72):27841–71. Available from: [<URL>](#).
- Hakki A, AlSalka Y, Mendive CB, Ubogui J, dos Santos Claro PC, Bahnemann D. Hydrogen Production by Heterogeneous Photocatalysis. In: Wandelt K, editor. Encyclopedia of Interfacial Chemistry [Internet]. Elsevier; 2018. p. 413–9. Available from: [<URL>](#).
- Dharma HNC, Jaafar J, Widiastuti N, Matsuyama H, Rajabsadeh S, Othman MHD, et al. A Review of Titanium Dioxide (TiO₂)-Based Photocatalyst for Oilfield-Produced Water Treatment. Membranes (Basel) [Internet]. 2022 Mar 19;12(3):345. Available from: [<URL>](#).
- Sharma PK, Cortes MALRM, Hamilton JWJ, Han Y, Byrne JA, Nolan M. Surface modification of TiO₂ with copper clusters for band gap narrowing. Catal Today [Internet]. 2019 Feb 1;321–322:9–17. Available from: [<URL>](#).
- Wei Y, Wu Q, Meng H, Zhang Y, Cao C. Recent advances in photocatalytic self-cleaning performances of TiO₂-based building materials. RSC Adv [Internet]. 2023 Jul 11;13(30):20584–97. Available from: [<URL>](#).
- Mimouni I, Bouziani A, Naciri Y, Boujnah M, El Belghiti MA, El Azzouzi M. Effect of heat treatment on the photocatalytic activity of α-Fe₂O₃ nanoparticles: towards diclofenac elimination. Environ Sci Pollut Res [Internet]. 2022 Jan 5;29(5):7984–96. Available from: [<URL>](#).
- Zhang H, Liu J, Xu T, Ji W, Zong X. Recent Advances on Small Band Gap Semiconductor Materials (≤2.1 eV) for Solar Water Splitting. Catalysts [Internet]. 2023 Apr 12;13(4):728. Available from: [<URL>](#).

19. Parthasarathy P, Vivekanandan S. Biocompatible TiO₂-CeO₂ Nano-composite synthesis, characterization and analysis on electrochemical performance for uric acid determination. *Ain Shams Eng J* [Internet]. 2020 Sep 1;11(3):777-85. Available from: [<URL>](#).
20. Cheng R, Xia J, Wen J, Xu P, Zheng X. Nano Metal-Containing Photocatalysts for the Removal of Volatile Organic Compounds: Doping, Performance, and Mechanisms. *Nanomaterials* [Internet]. 2022 Apr 13;12(8):1335. Available from: [<URL>](#).
21. Kusmierek E. A CeO₂ Semiconductor as a Photocatalytic and Photoelectrocatalytic Material for the Remediation of Pollutants in Industrial Wastewater: A Review. *Catalysts* [Internet]. 2020 Dec 8;10(12):1435. Available from: [<URL>](#).
22. Wang X, Wang J, Sun Y, Li K, Shang T, Wan Y. Recent advances and perspectives of CeO₂-based catalysts: Electronic properties and applications for energy storage and conversion. *Front Chem* [Internet]. 2022 Dec 8;10:1089708. Available from: [<URL>](#).
23. Tran DPH, Pham MT, Bui XT, Wang YF, You SJ. CeO₂ as a photocatalytic material for CO₂ conversion: A review. *Sol Energy* [Internet]. 2022 Jul 1;240:443-66. Available from: [<URL>](#).
24. Yang M, Shen G, Wang Q, Deng K, Liu M, Chen Y, et al. Roles of Oxygen Vacancies of CeO₂ and Mn-Doped CeO₂ with the Same Morphology in Benzene Catalytic Oxidation. *Molecules* [Internet]. 2021 Oct 21;26(21):6363. Available from: [<URL>](#).
25. Suman, Singh S, Ankita, Kumar A, Kataria N, Kumar S, et al. Photocatalytic activity of α -Fe₂O₃@CeO₂ and CeO₂@ α -Fe₂O₃ core-shell nanoparticles for degradation of Rose Bengal dye. *J Environ Chem Eng* [Internet]. 2021 Oct 1;9(5):106266. Available from: [<URL>](#).
26. Ranjbari A, Demeestere K, Kim KH, Heynderickx PM. Oxygen vacancy modification of commercial ZnO by hydrogen reduction for the removal of thiabendazole: Characterization and kinetic study. *Appl Catal B Environ* [Internet]. 2023 May 5;324:122265. Available from: [<URL>](#).
27. Paick J, Hong S, Bae JY, Jyoung JY, Lee ES, Lee D. Effective Atomic N Doping on CeO₂ Nanoparticles by Environmentally Benign Urea Thermolysis and Its Significant Effects on the Scavenging of Reactive Oxygen Radicals. *ACS Omega* [Internet]. 2023 Jun 27;8(25):22646-55. Available from: [<URL>](#).
28. Ishak N, Jeyalakshmi V, Setka M, Grandcolas M, Devadas B, Šoóš M. Upgrading of g-C₃N₄ semiconductor by a Nitrogen-doped carbon material: A photocatalytic degradation application. *J Environ Chem Eng* [Internet]. 2023 Apr 1;11(2):109381. Available from: [<URL>](#).
29. Yao C, Wang M, Jiang W, Chen Y. Study on a novel N-doped mesoporous carbon for the efficient removal of methylene blue from aqueous solution. *Environ Eng Res* [Internet]. 2020 Oct 27 [cited 2024 Jun 5];26(5):200339. Available from: [<URL>](#).
30. Jayakumar G, Irudayaraj A, Raj AD, Irudayaraj AA. Particle Size Effect on the Properties of Cerium Oxide (CeO₂) Nanoparticles Synthesized by Hydrothermal Method. *Mech Mater Sci Eng J* [Internet]. 2017;9(1). Available from: [<URL>](#).
31. Landi S, Segundo IR, Freitas E, Vasilevskiy M, Carneiro J, Tavares CJ. Use and misuse of the Kubelka-Munk function to obtain the band gap energy from diffuse reflectance measurements. *Solid State Commun* [Internet]. 2022 Jan 1;341:114573. Available from: [<URL>](#).
32. Yuan D, Liu Q. Photon energy and photon behavior discussions. *Energy Reports* [Internet]. 2022 May 1;8:22-42. Available from: [<URL>](#).
33. Ayyub MM, Rao CNR. Design of efficient photocatalysts through band gap engineering. In: Boukherroub R, Ogale SB, Robertson N, editors. *Nanostructured Photocatalysts* [Internet]. Elsevier; 2020. p. 1-18. Available from: [<URL>](#).
34. Wu B, Meng H, Morales DM, Zeng F, Zhu J, Wang B, et al. Nitrogen-Rich Carbonaceous Materials for Advanced Oxygen Electrocatalysis: Synthesis, Characterization, and Activity of Nitrogen Sites. *Adv Funct Mater* [Internet]. 2022 Aug 31;32(31):2204137. Available from: [<URL>](#).
35. Dao V, Cipriano LA, Ki SW, Yadav S, Wang W, Di Liberto G, et al. 2D/2D Z-scheme-based α -Fe₂O₃@NGr heterojunction implanted with Pt single-atoms for remarkable photocatalytic hydrogen evolution. *Appl Catal B Environ* [Internet]. 2023 Aug 5;330:122586. Available from: [<URL>](#).
36. Khani H, Khandan N, Eikani MH, Eliassi A. Investigation of synthesized Fe₂O₃ and CuO-Fe₂O₃ for pure hydrogen production by chemical-loop reforming of methanol in a micro-channel reactor. *Int J Hydrogen Energy* [Internet]. 2023 Feb 22;48(16):6436-50. Available from: [<URL>](#).